Supershear rupture of the 5 January 2013 Craig, Alaska (Mw 7.5) earthquake

Hua Yue, Thorne Lay, Jeffrey T. Freymueller, Kaihua Ding, Luis Rivera, Natalia A. Ruppert, Keith D. Koper

Supershear rupture of the 5 January 2013 Craig, Alaska (M_w 7.5) earthquake

Han Yue,[1] Thorne Lay,[1] Jeffrey T. Freymueller,[2] Kaihua Ding,[3] Luis Rivera,[4] Natalia A. Ruppert,[2] and Keith D. Koper[5]

Received 9 August 2013; revised 14 October 2013; accepted 21 October 2013; published 22 November 2013.

[1] Supershear rupture, in which a fracture's crack tip expansion velocity exceeds the elastic shear wave velocity, has been extensively investigated theoretically and experimentally and previously inferred from seismic wave observations for six continental strike-slip earthquakes. We find extensive evidence of supershear rupture expansion of an oceanic interplate earthquake, the 5 January 2013 $M_w = 7.5$ Craig, Alaska earthquake. This asymmetric bilateral strike-slip rupture occurred on the Queen Charlotte Fault, offshore of southeastern Alaska. Observations of first-arriving *Sn* and *Sg* shear waves originating from positions on the fault closer than the hypocenter for several regional seismic stations, with path calibrations provided by an empirical Green's function approach, indicate a supershear rupture process. Several waveform inversion and modeling techniques were further applied to determine the rupture velocity and space-time distribution of slip using regional seismic and geodetic observations. Both theoretical and empirical Green's functions were used in the analyses, with all results being consistent with a rupture velocity of 5.5 to 6 km/s, exceeding the crustal and upper mantle *S* wave velocity and approaching the crustal *P* wave velocity. Supershear rupture occurred along ~100 km of the northern portion of the rupture zone but not along the shorter southern rupture extension. The direction in which supershear rupture developed may be related to the strong material contrast across the continental-oceanic plate boundary, as predicted theoretically and experimentally. The shear and surface wave Mach waves involve strongly enhanced ground motions at azimuths oblique to the rupture direction, emphasizing the enhanced hazard posed by supershear rupture of large strike-slip earthquakes.

Citation: Yue, H., T. Lay, J. T. Freymueller, K. Ding, L. Rivera, N. A. Ruppert, and K. D. Koper (2013), Supershear rupture of the 5 January 2013 Craig, Alaska (M_w 7.5) earthquake, *J. Geophys. Res. Solid Earth*, *118*, 5903–5919, doi:10.1002/2013JB010594.

1. Introduction

[2] Seismological observations indicate that most earthquakes have an average rupture front expansion velocity slower than the elastic *S* wave velocity (subshear), typically at or below the medium Rayleigh wave velocity. However, both theoretically [*Burridge*, 1973; *Andrews*, 1976, 1985; *Burridge et al*., 1979; *Dunham et al*., 2003; *Dunham*, 2005; *Dunham and Bhat*, 2008] and experimentally [*Rosakis et al*., 1999; *Xia et al*., 2004; *Xia et al*., 2005; *Passelègue et al*., 2013], it is established that rupture can propagate faster than the *S* wave velocity (supershear) for mode II fractures with rupture propagation direction parallel to the fault slip direction, as is typical of strike-slip earthquakes. Dynamical models of supershear rupture indicate that high prestress and low static friction may be important to the initiation of supershear rupture process [*Burridge*, 1973]. The transition from subshear to intersonic (between *S* and *P* wave velocities) occurs when *S* wave energy ahead of the rupture front is sufficient to overcome frictional resistance on a preexisting fault surface, initiating a second rupture front ahead of a subshear front [*Andrews*, 1985; *Dunham and Bhat*, 2008; *Dunham et al*., 2003; *Festa and Vilotte*, 2006; *Liu and Lapusta*, 2008; *Kaneko and Lapusta*, 2010]. The supershear transition can be abetted by the existence of stress heterogeneity and by proximity to failure stress along the fault [e.g., *Day*, 1982; *Olsen et al*., 1997; *Dunham et al*., 2003; *Mena et al*., 2012].

[3] Geophysical inferences of supershear ruptures have been reported for six large strike-slip (mode II) earthquakes in continental crust and one strike-slip event within an oceanic plate [e.g., *Archuleta*, 1984; *Bouchon et al*., 2001; *Bouchon and Vallée*, 2003; *Choy and Boatwright*, 2004; *Frankel*, 2004; *Dunham and Archuleta*, 2004; *Robinson et al*., 2006;

Additional supporting information may be found in the online version of this article.

[1]Department of Earth and Planetary Sciences, University of California, Santa Cruz, California, USA.
[2]Geophysical Institute, University of Alaska Fairbanks, Fairbanks, Alaska, USA.
[3]Institute of Geophysics and Geomatics, China University of Geosciences, Wuhan, China.
[4]Institut de Physique du Globe de Strasbourg, Université de Strasbourg/CNRS, Strasbourg, France.
[5]Department of Geology and Geophysics, University of Utah, Salt Lake City, Utah, USA.

Corresponding author: T. Lay, Department of Earth and Planetary Sciences, University of California, Earth and Marine Sciences Bldg., 1156 High St., Santa Cruz, CA 95064, USA. (tlay@ucsc.edu)

2169-9313/13/10.1002/2013JB010594

Walker and Shearer, 2009; *Wang and Mori*, 2012]. The 1979 Imperial Valley M_S 6.9 earthquake was the first event for which supershear rupture was inferred [*Archuleta*, 1984]. By analyzing near-field data, an overall rupture velocity of 2.7–3.2 km/s was estimated [*Spudich and Cranswick*, 1984] with significant rupture velocity variation that included localized supershear rupture of a fault segment transected by nearby strong motion instruments [*Archuleta*, 1984]. In 1999, two strike-slip earthquakes struck the north Anatolian fault zone, the $M_w = 7.4$ İzmit and $M_w = 7.2$ Düzce events. Strong ground motions recorded directly along the Anatolian fault were used in source analyses, which indicate that both events had bilateral ruptures with supershear only on their eastern segments. A rupture velocity of ~5 km/s was reported for both events [*Bouchon et al*., 2001, 2002], close to the value of 1.414 times the shear velocity which is found to be a stable supershear rupture velocity in some theoretical calculations [*Freund*, 1979]. Additional studies of the Turkey events indicate a range of rupture velocity estimates, but all involve supershear rupture [e.g., *Sekiguchi and Iwata*, 2002; *Birgören et al*., 2004; *Bouin et al*., 2004; *Konca et al*., 2010]. Although ground motion amplification related to Mach waves is expected for supershear ruptures, ground motion simulations for supershear rupture models of the İzmit event did not produce significant peak ground velocity enhancements [*Aochi et al*., 2011], likely because the length of supershear rupture was fairly short.

[4] The 2001 M_w 7.8 Kokoxili (Kunlunshan), China event appears to have had a more extensive supershear rupture. Although on-fault observations are not available for the Kokoxili event, eastward rupture along a 300 km long segment produced significant directivity effects, allowing supershear rupture to be identified in seismic data collected at regional distances (<2000 km) [*Bouchon and Vallée*, 2003]. Mach waves produced by the supershear rupture segment have coincident arrivals from the finite-source toward particular directions [*Vallée and Dunham*, 2012] and exhibit significant amplitude enhancement due to constructive interference. Supershear rupture of the Kokoxili event is also apparent in teleseismic *P* wave back projections [*Walker and Shearer*, 2009], which indicate an initial subshear rupture velocity over a distance less than 40 km, then increase to supershear rupture velocity of ~5.6 km/s.

[5] Using teleseismic back projections, *Walker and Shearer* [2009] also identified a similar rupture process for the 2002 M_w 7.9 Denali, Alaska event. For the Denali event, one strong motion station, deployed 3 km from the fault, recorded unusual ground motions attributed to supershear rupture based on dynamic source simulations [*Ellsworth et al*., 2004; *Dunham and Archuleta*, 2004]. A strong Mach wave and a trailing fault surface Rayleigh wave were detected in the near-field record; this complexity has also been observed in laboratory experiments [*Mello et al*., 2010]. The moderate size M_w 6.9 2010 Yushu, China earthquake is the smallest event interpreted as having supershear rupture, based on one near-field observation along the fault and teleseismic short-period waveform back projections [*Wang and Mori*, 2012]. The rupture is relatively short, so teleseismic inferences of supershear rupture are marginal for events of this size.

[6] The 2012 M_w 8.6 Indo-Australia intraplate oceanic earthquake is the largest strike-slip event yet observed [*Yue et al*., 2012]. The rupture process of the Indo-Australia event is very complex, involving rupture of no less than four segments. No near-field data are available, but supershear rupture was inferred using teleseismic *P* wave back projections in one study [*Wang et al*., 2012] while other back projections indicate relatively low rupture velocities [*Meng et al*., 2012; *Yue et al*., 2012]. The evidence for supershear rupture of this event is marginal despite its size, mainly due to the complexity of the process. Generally, rupture velocity is easier to determine for a long unilateral rupture like the Kokoxili event [e.g., *Antolik et al.*, 2004; *Bouchon and Vallée*, 2003] or when near-regional ground motion recordings are located directly along the fault rupture as for the Imperial Valley, Denali, İzmit, Düzce, and Yushu events [e.g., *Bouchon et al*., 2001; *Dunham and Archuleta*, 2004].

[7] Supershear rupture produces horizontally expanding planar *S* and surface wave Mach waves that enhance ground shaking and damage at small oblique angles to the direction of rupture propagation, affecting wave energy distribution [*Das*, 2007; *Kaneko and Lapusta*, 2010; *Andrews*, 2010]. Near the Mach cone azimuth, which is determined by the rupture velocity, the waves from along the supershear portion of the rupture interfere constructively to resemble the plane waves, effectively spreading from a line source rather than a point source, giving significantly enhanced amplitude [*Vallée and Dunham*, 2012]. The strong directivity effect of supershear rupture may cause severe damage in the forward rupture direction [*Das*, 2007; *Wang and Mori*, 2012]. For several supershear events, aftershock distributions have been found to be absent on the supershear rupture segment but abundant in splay faults. This may be caused by nearly total stress release on the main fault plane with the branch fault being activated by significant ground shaking and static stress loading [*Bouchon and Karabulut*, 2008]. Occurrence of supershear rupture is thus important for ground shaking modeling and seismic hazard estimation, along with revealing fundamental physics of rupture initiation.

2. The 2013 M_w 7.5 Craig, Alaska Strike-Slip Earthquake

[8] On 5 January 2013, a large strike-slip event struck along the Queen Charlotte Fault (QCF) offshore of southeastern Alaska (55.4°N, 134.7°W, depth = 10 km, 08:58:19 UTC; http://comcat.cr.usgs.gov/earthquakes/eventpage/pde20130105085819330_10#summary). This is called the Craig, Alaska earthquake. The fault is the main plate boundary between the Pacific (oceanic) and North America (continental) plates and experiences right-lateral shearing on a steeply dipping plane at a long-term rate of about 47 mm/yr. The strike-slip focal mechanism (Figure 1) of the 2013 event is consistent with shallow rupture of the plate boundary. Approximately 300 aftershocks within 1 month after the main shock were located by the Alaska Earthquake Information Center (AEIC) and are distributed ~100 km to the north and ~30 km to the south of the epicenter, indicating an asymmetric bilateral rupture with predominantly northward extension. The earthquake seismic moment is ~2.2×10^{20} Nm and the magnitude is M_w 7.5 [*Lay et al*., 2013]. Supershear rupture has been reported for comparable size earthquakes, such as the M_w 7.6 1999 Izmit earthquake [*Bouchon et al*., 2001], but the offshore location of the 2013 Craig, Alaska earthquake precluded near-fault

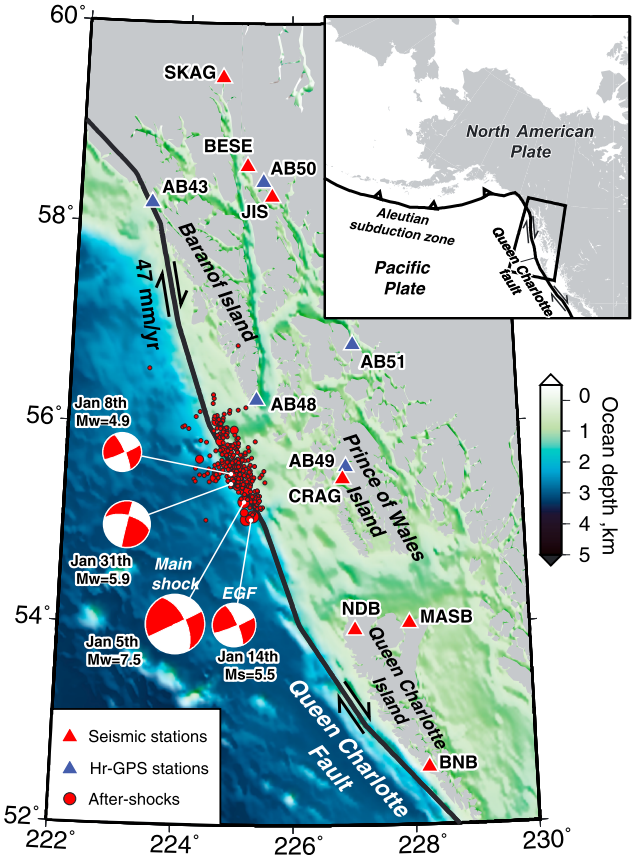

Figure 1. The inset indicates the regional plate tectonic setting with the Pacific and North America plates shearing horizontally at 47 mm/yr (black arrows) along the Queen Charlotte Fault (black line) and converging along the Aleutian trench. The map shows the focal mechanism solutions of the 5 January 2013 (M_w 7.5) main event and three aftershocks. The 14 January 2013 (M_w 5.5) aftershock is used to provide empirical Green's functions (EGFs) in the pre-hypocentral *S* wave and Mach wave analyses. The 31 January 2013 (M_w 5.9) event is also used as an EGF in the pre-hypocentral *S* wave analysis. Near-field high-rate GPS and seismic stations are shown as blue and red solid triangles, respectively. The locations of aftershocks in the first month following the main shock are small red solid circles.

ground motion measurements. Fortunately, the fault runs along the continental margin, and numerous seismic and geodetic stations in Alaska and western Canada located at near-regional (<400 km) to regional distances (<1500 km) provide >180° azimuthal coverage of seismic radiation and static ground deformation for the event.

3. Direct Supershear *S* Wave Observations

[9] The most straightforward evidence for a supershear rupture is observation of *S* waves at positions along the rupture direction that arrive earlier than the *S* wave from the hypocenter, with ensuing arrivals coming in reverse chronological order of the rupture process. Figure 2 shows that for a subshear rupture, the initial shear wavefront arriving at all directions originates from the hypocenter. For a supershear rupture, the rupture front precedes the *S* wavefront from the hypocenter at azimuths near the rupture direction, producing initial arrivals (designated pre-hypocentral *S* waves) from the end of the supershear segment at small oblique angles to the rupture propagation direction. At larger oblique angles in the forward rupture direction, the energy from the entire rupture sequence arrives together, constituting a locally planar *S* Mach wave. Such Mach waves are observed in supershear rupture experiments using laser image snapshots [*Rosakis et al.*, 1999; *Xia et al.*, 2004, 2005] or recorded accelerograms [*Passelègue et al.*, 2013], providing the main supershear detection criteria in experimental measurements. However, it is challenging to identify such a Mach wave for earthquakes, because the wavefront from the hypocenter is always distorted by local structure heterogeneities (Figure 2c), and the distribution of seismic stations is usually inadequate to resolve the continuous wavefront. The detailed velocity structure controlling the arrival times is usually not well known; therefore, it is difficult to precisely calculate the hypocentral *S* arrival time to differentiate it from any pre-hypocentral *S* wave. Furthermore, regional *S* wave signals tend to be very complex due to crustal waveguide interactions, making it difficult to identify pre-hypocentral arrivals and Mach waves.

[10] To address these challenges, we use signals from a 14 January 2013 (M_w 5.5) aftershock (Figure 1) as empirical Green functions (EGFs). This small event has negligible rupture complexity and short-period regional *S* wave (*Sg*) arrivals can be picked reliably at stations that also record the main shock. Because the EGF event locates close to the main event hypocenter, the EGF wavefront resembles the shape of main event hypocentral wavefront even though distorted by propagation effects (Figure 2d). After determining the relative location of the two hypocenters, we correct for the *Sg* or *Sn* arrival time differences expected due to the differential hypocenter locations, aligning waveforms for both events, which effectively aligns the EGF *Sg* or *Sn* wavefront with the corresponding main event hypocentral wavefront (Figure 2d). Then, observation of any significant energy ahead of the hypocentral/EGF arrivals can be attributed to supershear rupture of the larger event.

3.1. EGF Relocation

[11] Precise relative locations of the EGF and main shock hypocenters are needed for our analysis. We manually measured the initial *Pn* phase arrival times of both the main shock and the EGF event at regional stations. The differential travel times from 26 stations located within 1000 km are used in our relative location determination, with both southern and northern stations being important for constraining the along-fault location (Figure 3). We held the main shock location fixed at 55.2280°N, −134.8591°E, 10 km deep, as located by the AEIC using regional networks. The initial time of the main shock is 08:58:15 in the AEIC catalog, which is 4 s earlier than the initial time reported by the USGS National Earthquake Information Center. Such an origin time discrepancy originates from differences in velocity models or differences in picking of small initial phase arrivals. The USGS location predicts ~3 s arrival time discrepancies with the closest stations, so for the regional data, we prefer the AEIC parameters. Only *Pn* phase data are used in our relative relocation, since the shear wave phases may be influenced by supershear rupture effects.

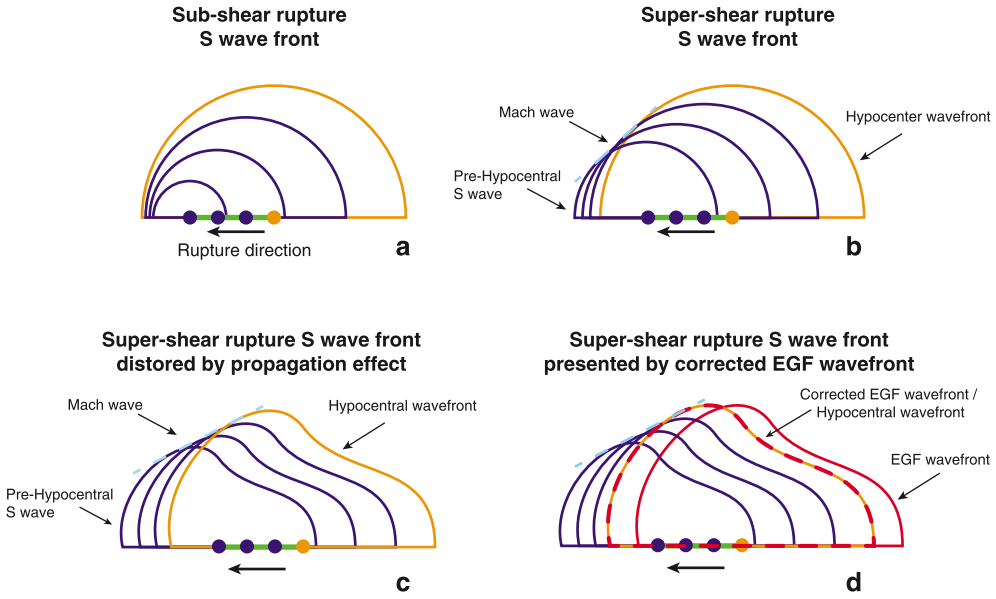

Figure 2. (a) The *S* wavefronts from the hypocenter and three locations along the leftward propagating rupture front are indicated by orange and blue semicircles, respectively. For subshear rupture velocity, the initial *S* wave observed at all locations originates at the hypocenter. (b) In a supershear rupture, the *S* wave arrives earlier than the hypocentral wavefront along the rupture propagation direction and a Mach wave (cyan dashed line) develops at oblique angle to the rupture direction. (c) For actual earthquakes, the rupture front is always distorted by heterogeneities, which makes it difficult to identify any pre-hypocentral arrival or a Mach wave, which will be distorted from planar by the heterogeneities. (d) The EGF wavefront (red curve) resembles the shape of the main shock hypocentral wave front (orange curve), because the signals travel through similar structures. When corrected for the differential arrival times due to the epicentral shift for the corresponding specific phase, the EGF wavefront (red dashed curves) closely matches the main shock hypocentral wavefront. Because the EGF wavefront is easier to identify, this operation helps to detect any pre-hypocentral *S* wave arrivals and Mach cone behavior for stations in the supershear rupture direction.

[12] The *Pn* differential arrival times are calculated through a 1-D layered model, extracted from a nearby active source reflection profile that includes a velocity contrast across the oceanic/continental plate boundary [*Horn et al.*, 1984]. Given that the near-field stations are all located on the landward side and the raypaths all traverse landward structure, we averaged the velocity structure on the landward side to obtain the 1-D structure shown in Table 1. A *Vp*/*Vs* ratio for layered structure obtained from a nearby receiver function study [*Morozov et al.*, 1998] is used to estimate *S* wave velocities from the *P* wave velocities.

[13] A classical Newton inversion method was applied to search for the relative location and initial time of the EGF event, avoiding local minima effects by using multiple initial locations. The relocated EGF hypocenter is 55.0469°N, 134.7303°E, about 20 km southeast of the main shock hypocenter. The main shock and EGF are assumed to be at the same depth because in *Pn* phase location the initial time trades-off with the hypocenter depth. The average differential time residual is <0.5 s, which indicates relative location error of <4 km (Figure 3). The lack of stations to the west limits resolution of the location in the EW direction, but the similarity of the focal mechanisms for the EGF and main shock (Figure 1) indicates that they are both on the Queen Charlotte Fault. A summary of main shock and aftershock locations is shown in Table 2. We also list the AEIC location of the 31 January 2013 M_w 5.9 event, which we used as a second EGF (EGF2) for regional *S* wave analysis.

3.2. *Sg* Wave Alignment and Pre-hypocentral *Sg* Wave Observations

[14] With the relative locations between the main shock and EGF being well determined, we can shift the *Sg* arrival time of the EGF signals to correspond to the main shock hypocenter using our 1-D velocity model and corresponding computed *Sg* raypaths. Because the distance between the relative hypocenters is small, ~20 km, the *Sg* travel time error produced by correcting for the differential path length to each station is <0.5 s, even allowing for 10% inaccuracy in the reference model. After correcting to a common hypocenter, the EGF waveforms identify when signals from the main shock hypocenter should arrive in the main shock waveforms. The arrival time of the relatively simple *Sg* phases for the shifted EGF waveforms is picked and both sets of signals are aligned on the hypocentral phase arrival times. The waveforms are filtered with a causal band-pass filter with corner frequencies of 1 and 10 Hz to remove low-frequency energy from preceding *Sn* phases and to emphasize the *Sg* arrivals.

[15] Figure 4 shows that the main shock and EGF hypocentral short-period vertical component *Sg* arrivals are well aligned at the southern stations, FSB, BNB, MASB, and NDB, but the main shock has clear large amplitude arrivals before the hypocentral *Sg* arrival at the northern stations JIS and BESE. Corresponding energy is not present in the EGF waveforms, reducing the possibility of any propagation effect such as *P* wave scattering or multipathing, which should be in

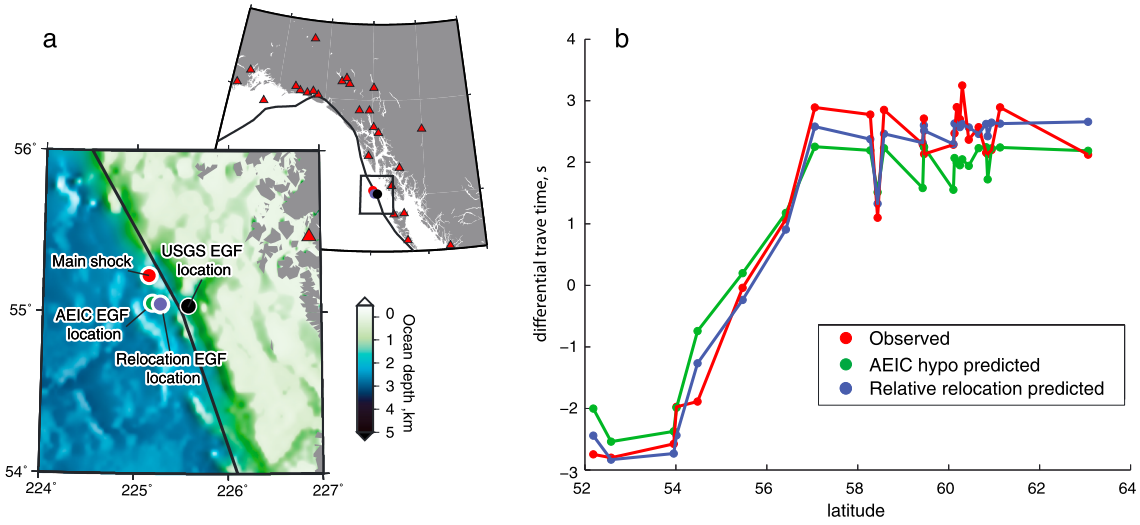

Figure 3. (a) In the inset, positions of stations used for relative location are shown as red solid triangles. In the main map, the AEIC main shock location, AEIC and USGS reported EGF locations, and our relocated relative EGF location are plotted with red, green, black, and blue solid dots, respectively. The Queen Charlotte Fault is plotted with a black solid line. (b) Differential *Pn* wave arrival times between the main shock and the EGF event at each station sorted by their respective latitude. The curves are the observed differential arrival times (red), the predicted differential arrival times for the AEIC location (green), and for our relative relocation (blue).

common for both sources. We attribute this energy to supershear rupture. For more distant northern stations, the *Sg* waves are not confidently identified in the EGF waveforms so this procedure cannot be applied to more data.

[16] We also made similar *Sg* waveform comparisons of the main shock and EGF recordings for various band-passes for tangential component ground displacements. Because the close southern stations on Haida Gwaii, including BNB, MASB, and NDB, are all short-period (< 1 s) vertical component stations, only stations to the north are used for the tangential component analysis. A similar hypocentral equalization process was also applied to records for EGF2, for which we corrected for the *Sg* arrival time caused by the differential locations reported by AEIC (Table 2). The comparison of the main shock, EGF, and EGF2 tangential displacement *Sg* arrivals is summarized in Figure 5a. The main shock broadband tangential components at northern stations consistently show 3 to 5 s early initial *Sg* arrivals to the north relative to both EGF and EGF2, compatible with the results in Figure 4. This is apparent in all bandwidths for the tangential component signals.

[17] The main shock/EGF amplitude ratios of the *Sg* signals in Figure 4 show 1 order of magnitude difference between the southern and northern stations, indicating a strong directivity effect of the main shock rupture process. It proves difficult to fully model the short-period amplitude ratios because of the uncertain propagation effects, as discussed below.

3.3. *Sn* Wave Alignment and Pre-hypocentral *Sn* Wave Observations

[18] *Sn* waves refract along the continental crust-mantle (Moho) boundary and arrive earlier than the *Sg* phase at regional distances, with lower frequency content (Figure 5). If the rupture velocity surpasses the upper mantle shear velocity (~4.5 km/s), we should also observe a pre-hypocentral *Sn* arrival at the northern stations. We corrected the *Sn* phase arrival times in EGF waveforms for the differential path lengths relative to the main shock, using the *Sn* slowness for our 1-D model. The waveform comparisons, again aligned on the hypocentral arrival for the main shock and EGF, are shown in Figure 5b, for two high-quality recordings. Here we use relatively broad band-pass filters to capture the low-frequency content of the *Sn* headwaves. The main shock has ramp-like onsets of *Sn* for which it is difficult to measure absolute arrival times, but the EGF signals have sharper onsets and the differential times can still be confidently measured. The main shock *Sn* initial phases arrive about 5 s earlier than the hypocentral *Sn* time, similar to the *Sg* data. As tangential component *Sn* is the first expected arrival on the tangential components, these observations are not subject to possible contamination from earlier *S* arrivals (whereas *Sn* precedes *Sg* in the data in Figures 4 and 5a).

[19] With this EGF alignment technique, we have clearly identified *Sn* and *Sg* waves that arrive earlier than the hypocentral *Sn* and *Sg* shear waves. These observations clearly demonstrate the existence of supershear rupture. Since pre-hypocentral waves are observed in both *Sg* and *Sn* phases, the rupture velocity exceeds both the crustal and upper mantle shear velocity and thus is >4.5 km/s. The initial pre-hypocentral arrivals originate from the terminus of the

Table 1. Regional 1-D Velocity Model

Layer Thickness (km)	*Vp* (km/s)	*Vs* (km/s)	Density (kg/m^3)
7.0	6.30	3.53	2600
8.0	6.50	3.54	2790
7.0	6.50	3.56	2900
6.0	6.80	3.67	3000
22.0	7.80	4.50	3500
Inf	8.10	4.50	3500

Table 2. Earthquake Locations

Event	Date	Time (UTC)	Latitude	Longitude	Depth (km)	M_w	Source of Information
Main shock	5 Jan	08:58:15	55.228	−134.859	10	7.5	AEIC
EGF1	14 Jan	18:45:49	55.047	−134.730	10	5.5	Relocated
EGF2	31 Jan	09:53:43	55.437	−134.963	14	5.9	AEIC

supershear rupture segment, but locating that depends on the rupture expansion history of the event. Fully quantifying the rupture velocity history requires constraints on the spatiotemporal slip distribution along the fault, which must be determined using azimuthally distributed observations.

4. Finite-Fault Model Inversion

[20] Space-time evolution of a large earthquake rupture is usually determined by finite-fault model (FFM) inversion, quantifying the rupture velocity, *Vr*, and slip distribution. Supershear rupture velocity has been identified using FFM inversion for some previous events [e.g., *Bouchon et al.*, 2002; *Konca et al.*, 2010]. Joint inversions including near-regional ground motions provide improved sensitivity to the rupture velocity compared to using only teleseismic data sets [*Yue and Lay*, 2013; *Yue et al.*, 2013]. Thus, we include both teleseismic and near-field seismic and geodetic records in our FFM inversion. Ground motion recordings at near-regional epicentral distances <400 km from the 2013 event are available from five high-rate GPS (hr-GPS) stations and three broadband seismic stations (Figure 5). Resolving *Vr* still depends on the geometry of the station distribution, which is one-sided for the 2013 Craig, Alaska event, with most stations being located along the northern extent of the rupture. Fortunately, the rupture is predominantly toward the north. For a well-determined hypocenter and good regional velocity model, the main parameter controlling the initial *S* wave arrival time for any northward supershear radiation at stations along the rupture is the rupture velocity. For stations in the south, the initial motion comes from the hypocenter, so the rupture velocity does not affect the timing of the initial motion.

4.1. Model Parameterization

[21] The finite-fault model is parameterized with 16 nodes along strike with 10 km increments and 3 nodes along dip with 5 km increments (Figure 6). The total size of the FFM is 160 km along strike and 15 km along dip. The strike is 335° and dip is 63°, given by the USGS W-phase point source focal mechanism. We found that this geometry fits the data slightly better than using the global centroid moment tensor (g-CMT) solution, but using the g-CMT solution does not produce significant differences in rupture velocity or slip patterns. The hypocenter is 45 km from the southern end of the model and 115 km from the northern end. We use a multi time-window linear inversion technique [*Hartzell and Heaton*, 1983], in which the source time function of each subfault is parameterized with eight symmetric triangles with 2 s rise times and 2 s shifts, allowing up to 18 s long source time functions for each subfault. We use two slip-vector orientations for each subfault to allow rake-varying slip, applying a nonnegative least squares inversion [*Lawson and Hanson*,

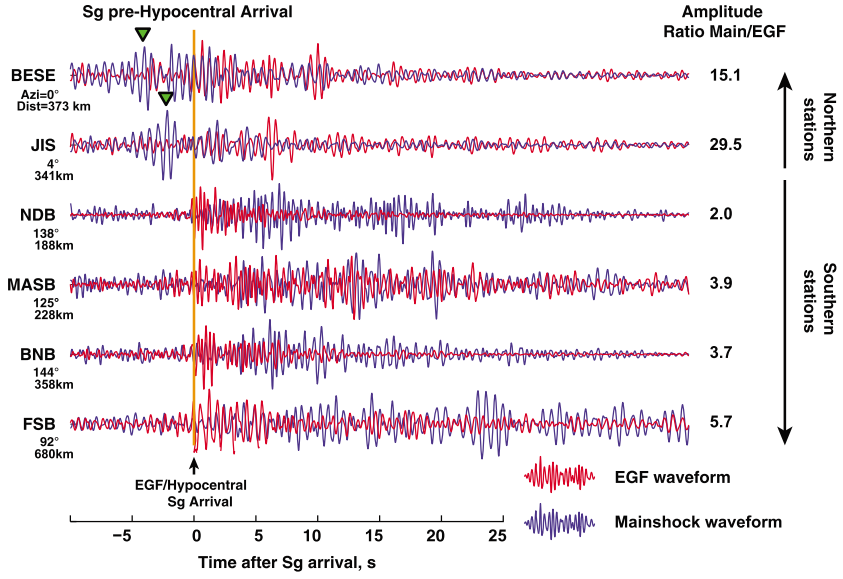

Figure 4. Regional vertical component seismic records of the main shock (blue traces) and the EGF event (red traces) aligned on the manually selected *Sg* arrivals from the EGF. All records are band-pass filtered between 1 and 10 Hz and normalized by their maximum amplitudes. Station names, azimuths, and distances are indicated along with observed ratios of peak *Sg* amplitudes (main shock/EGF). For the northern stations, very large *Sg* arrivals for the main shock (green solid triangles) arrive earlier than arrivals from the hypocenter, requiring close source locations that can only be reached by supershear rupture, as in the example in Figure 2.

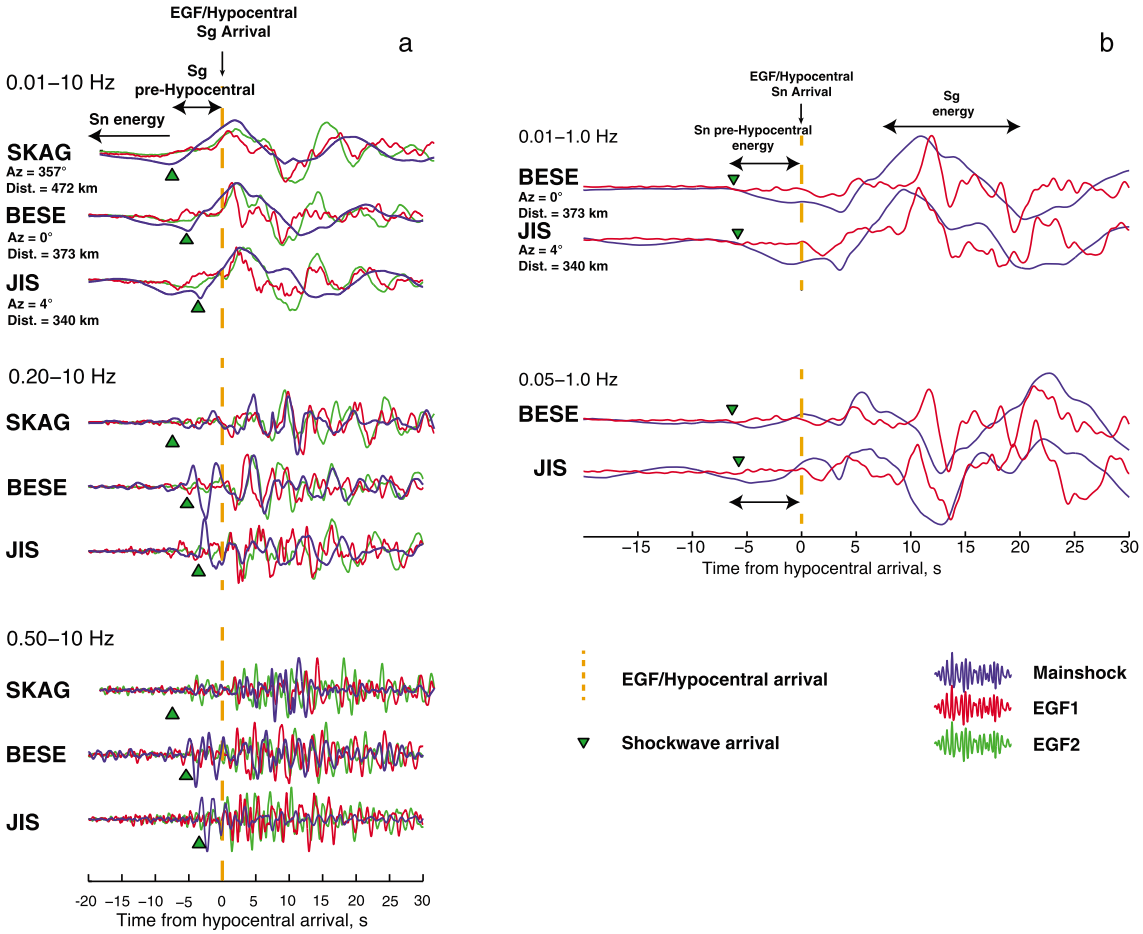

Figure 5. (a) Regional tangential component ground displacement records of the main shock (blue traces) and the two EGF events (red traces and green traces) aligned on the manually selected *Sg* arrivals from the EGFs for station BESE. Records are band-pass filtered between 0.01–10, 0.2–10, and 0.5–10 Hz and normalized by their maximum amplitudes. Station names, azimuths, and distances are indicated. The stations shown here locate north of the hypocenter. The hypocentral/EGF *Sg* arrivals are aligned at 0 s and marked with an orange dashed line. The *Sg* pre-hypocentral arrivals for the main shock traces are marked with green solid triangles. (b). Regional tangential component ground displacement records of the main shock (blue traces) and the EGF1 event (red traces) aligned on the manually selected *Sn* arrivals from the EGF. Records are band-pass filtered between 0.01–1.0 and 0.05–1.0 Hz and normalized by their maximum amplitudes. Station names, azimuths, and distances are indicated. Stations locate to the north of the hypocenter. The hypocentral/EGF *Sn* arrivals are aligned at 0 s and marked with an orange dashed line. The *Sn* pre-hypocentral energy arrivals are marked with green solid triangles.

1995] in which the rake of each subfault is allowed to vary between 135° and 225°. We apply Laplacian regularization, which constrains the second order gradient for each parameter to be zero.

[22] Three data sets are used in the FFM inversions: near-regional hr-GPS, near-regional seismic, and teleseismic data. The near-regional records are all from stations located within 400 km of the hypocenter. For these, we use 1-D Green functions computed for our regional model.

4.2. Hr-GPS Data Set

[23] We used five hr-GPS stations with three-component recordings of full ground displacements including time-varying seismic motions and static offsets. The GPS stations are part of the Earth Scope Plate Boundary Observatory, operated by UNAVCO. We produce displacements from 1 sample per second GPS phase and pseudorange observations in a PPP solution [*Zumberge et al.*, 1997] with the GIPSY software and JPL final orbits and clocks. The JPL clock estimates were linearly interpolated from 30 s to 1 s sampling. We estimate position variations using a random walk noise model in GIPSY's Kalman filter; aside from the kinematic solution approach, other models applied were the same as those used for daily position estimates [*Fu and Freymueller*, 2012]. This process produces a position time series for each site in the ITRF2008 reference frame. A sidereal filter was applied to each record to remove the noise introduced by local multipathing, and we used the 20 min before the earthquake to define the zero point for the displacement seismograms.

[24] For inversion, the hr-GPS data are filtered with a causal low-pass Butterworth filter with a corner frequency

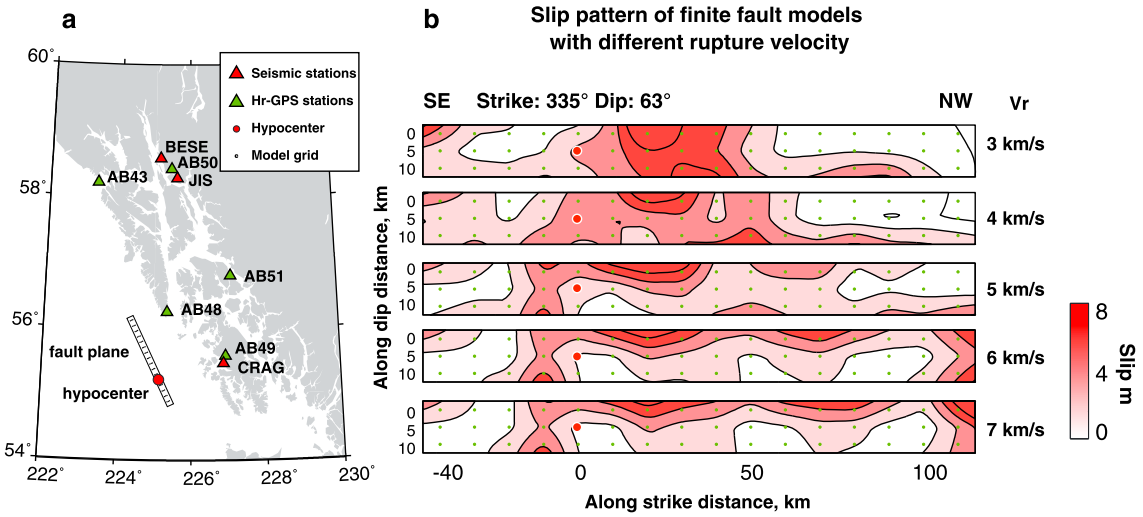

Figure 6. (a) Hr-GPS and seismic station locations are shown as green and red solid triangles. Three component ground motions from each station are inverted jointly with teleseismic *P* and *SH* waves to give finite fault models for slip distribution. The model grids are shown as black dots along the rectangle with the hypocenter location marked as a red dot. (b) Slip pattern of finite fault models inverted with different prescribed rupture velocities, *Vr*. Grid points and the hypocenter are shown as green and red solid dots, respectively. Magnitude of the predominantly right-lateral slip is contoured for each case.

at 0.2 Hz. A 160 s time window is applied to the data spanning the dynamic waveforms and static ground displacements in all records. The same low-pass filter is applied to the Green's functions. The Green's functions are generated by a frequency-wave number integration method including all near-field terms (Robert Herrmann, Computer Programs in Seismology). The velocity structure is that in Table 1. We also used Green's functions for a model with a 3 km thick water layer. The latter inversion results are not significantly different and are not included in this paper. The vertical components are downweighted by a factor of 0.2 to compensate for the higher noise level in the vertical records.

4.3. Near-Regional Seismic Data Set

[25] We used three near-regional broadband seismic stations with three component recordings from the Alaska Regional Seismic Network (ARSN). The instrument responses were removed to recover ground displacements filtered with a causal band-pass filter in a band of 0.02–0.2 Hz. A 200 s long time window was used for the seismic data, spanning the main seismic energy in these records. The F-K integration algorithm was used to compute Green's functions for the seismic data. The same band-pass filter was applied to the Green's functions.

4.4. Teleseismic Data Set

[26] Ninety-three teleseismic records were used in the joint inversion, including 64 *P* wave and 29 *S* wave records, from global stations of the Federation of Digital Seismic Networks (FDSN), accessed through the Incorporated Research Institutions for Seismology (IRIS) data center. The data were selected from hundreds of available FDSN seismograms to have good azimuthal coverage (Figure S1 in the supporting information) and high signal-to-noise ratios for epicentral distances from 40° to 90°. The instrument responses were removed from the raw data to recover ground displacement records. A causal band-pass filter in a band 0.005–0.9 Hz was applied to the data. To align with the absolute time of the local data, the teleseismic *P* wave onsets were shifted by 4 s, as the visible initial motion of the teleseismic records is consistent with the 4 s late initial time reported by the USGS-NEIC. The teleseismic Green's functions were generated with a reflectivity method that accounts for interactions in 1-D layered structures on both the source and receiver sides [*Kikuchi et al.*, 1993]. A 3 km deep water layer was added to the 1-D source region structure to compute the teleseismic surface reflected phases accurately. A 90 s long data window with 10 s leader before the initial motion was used. The *S* waves were downweighted by a factor of 0.2 to compensate for the very large *S* wave amplitudes.

4.5. Inversion Results

[27] In multi time-window inversion, a maximum rupture velocity (*Vr*) is imposed, so inversions were conducted for different values of *Vr*. In all cases shown here, the rupture initially expands bilaterally at a subshear velocity of 3 km/s to 20 km from the hypocenter, and then *Vr* increases to a specified value, ranging from subshear to supershear (3 to 7 km/s), on the northern segment. As *Vr* on the northern segment increases, the spatial extent of the slip pattern expands (Figure 6), leading to significant improvements in waveform fitting (Figures 7 and S1). If the prescribed *Vr* exceeds the actual rupture velocity and the data are sufficient to spatially resolve the slip distribution, the slip pattern stabilizes, and the waveform fitting residual has no significant reduction with further *Vr* increase. For our FFM inversions, the slip models and waveform misfit stabilize for $Vr = 5.5$ to 6.0 km/s (Figure 7c), indicating that range as a reasonable upper bound on rupture expansion velocity. We find that the results do not depend strongly on the assumed initial subshear velocity or the length for the first stage of subshear rupture. The acceptable *Vr* of 5.5 to 6 km/s is supershear

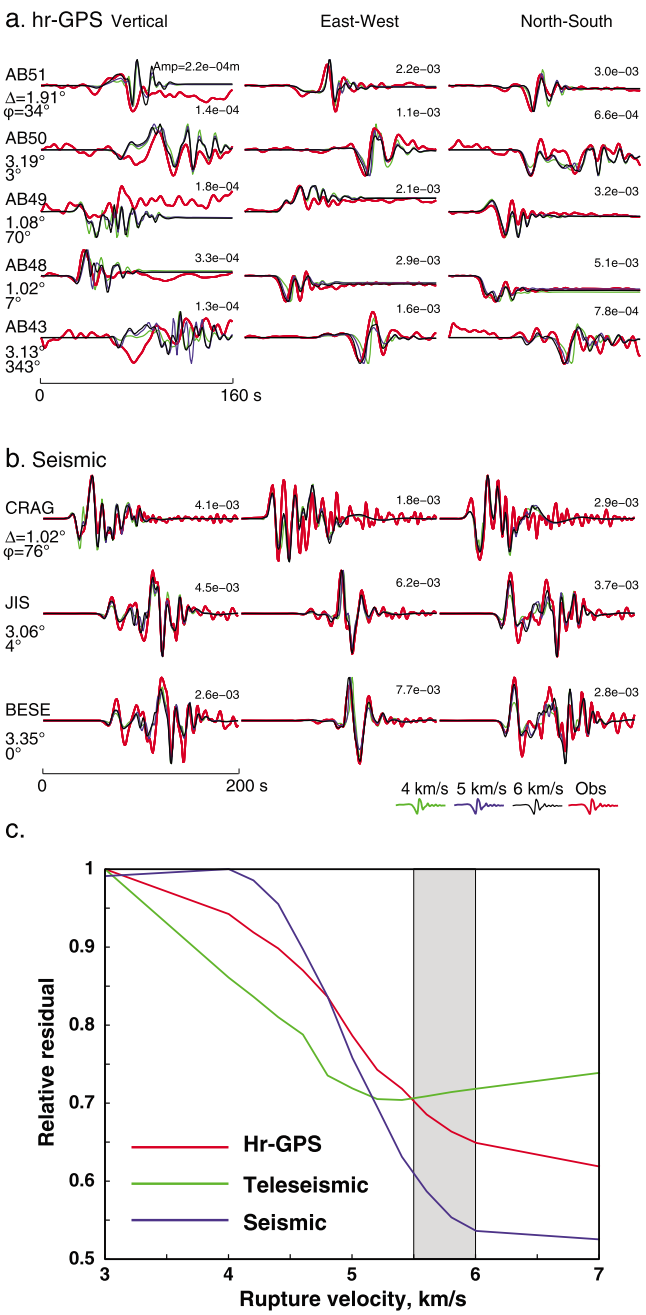

Figure 7. Representative observed and predicted waveforms for finite-fault models are shown for (a) hr-GPS records and (b) near-regional seismic records. Three-component records are used and shown in columns. In both cases, observed waveforms are plotted in red, and modeled waveforms for input rupture velocity of $Vr = 4.0$, 5.0 and 6.0 km/s are plotted in green, blue, and black, respectively. Station names, epicentral distances, and azimuth of each record are labeled for each case. (c) Trade-off curves indicating normalized inversion residual versus assumed rupture velocity for each data set for joint inversions. Red, blue, and green curves are normalized residuals of hr-GPS, seismic, and teleseismic data sets, respectively. The range of preferred rupture velocity (5.5–6.0 km/s) is shaded. All observed waveforms and inversion predictions are shown in Figure S1.

relative to the local crustal *S* wave velocity of 3.8 km/s and upper mantle *S* wave velocity of 4.5 km/s [*Morozov et al.*, 1998], compatible with the *Sn* and *Sg* pre-hypocentral arrival observations. The FFM inversions indicate that the fault slip extends from the seafloor to ~15 km deeper, extending below the oceanic crust (~6 km thick) to the west but still against the continental crust (~25 km thick) to the east. For our preferred FFM rupture model ($Vr = 6$ km/s; Figure 6b), the slip distribution extends ~110 km to the north and ~40 km to the south of the hypocenter. The northern terminus of the rupture is not tightly constrained, and we specify it based on the aftershock distribution. Two large slip patches are located ~20 km and ~70 km north of the hypocenter; the maximum slip of these two patches is from 8 to 10 m, varying slightly with different input parameters, but the locations of these two patches are stable. The total seismic moment is 3.2×10^{20} Nm, corresponding to M_w 7.6.

5. Linear Fault Model Inversion

[28] Effects of errors in the velocity structure increase as distance to a recording station increases, making it difficult to include regional seismic data beyond 400 km distance in the FFM using theoretical Green's functions. In FFM inversions, the rupture velocity can trade off with model velocity, such that apparent supershear *Vr* could be produced as an artifact of having too low of a velocity model. To overcome the uncertainty of the regional wave propagation, we use broadband Love and Rayleigh surface waves from the 14 January 2013 (M_w 5.5) aftershock as EGFs to invert for the rupture process. The EGF waveforms account for the first-order complexity of surface wave propagation along the path from the source to each regional station. EGF-based waveform inversion will diminish the potential bias caused by inaccurate wave propagation effects, enhancing sensitivity to the along-strike source rupture process.

5.1. Empirical Green's Function Corrections

[29] In the EGF analysis, the path to each station for the EGF event is similar to that for each position along the main shock rupture, except for differences in path length near the source region (Figure 8). Assuming that the EGF and the main shock have the same average focal mechanism, giving identical initial phase at a particular azimuth, the phase difference between the EGF and the Green's function for any node on the main shock model is proportional to the differential propagation distance. Assuming the heterogeneity of structure from the EGF to the main shock nodes is small, we use the local 1-D model to correct for the phase differences, giving empirical Green's function at each model node as perturbations of the EGF waveforms (Figures 8b and 8c). High-frequency data may not be well corrected in this way, since at regional distances the high-frequency energy involves body waves with multiple interfering phases with different slowness. But the low-frequency energy of the regional records is mainly fundamental surface waves that can be corrected with a dispersion curve.

[30] Our phase velocity correction technique involves the following steps:

[31] 1. The spectra of the EGF waveforms are computed from the recorded waveforms.

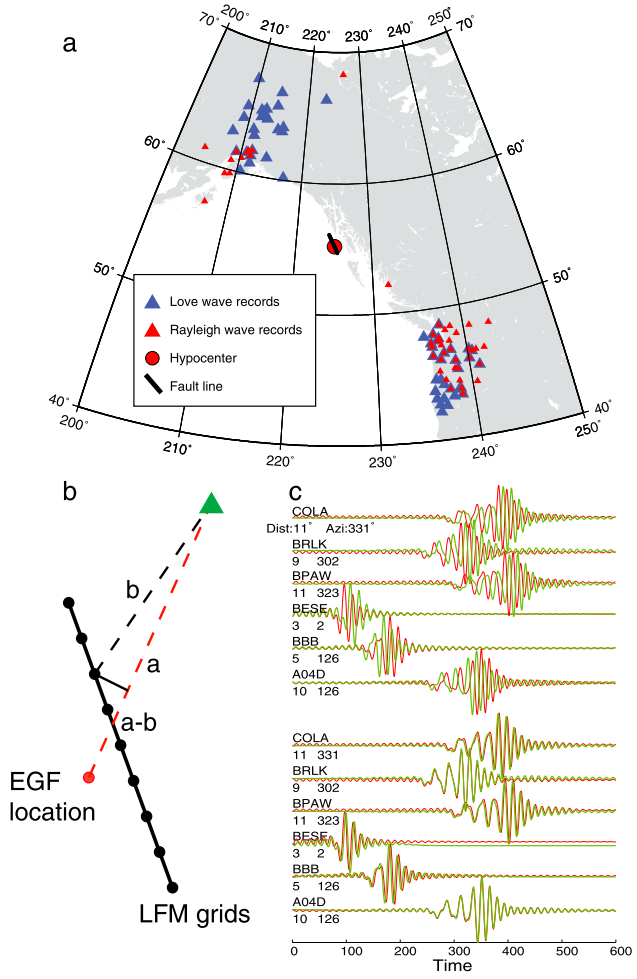

Figure 8. (a) Regional distance stations used for linear fault model inversions and forward modeling of Love and Rayleigh waves. Stations providing G1 and R1 records are shown as red and blue triangles, respectively. Stations locate within 30° from the nodal directions are excluded in both data sets. The linear fault plane is marked with a black solid line, and the hypocenter is marked with a red solid dot. (b) For a station at regional distance, the EGF wave path length a, and the path length from a model node b differ as a function of the station location. After correcting the EGF phase spectrum at each station for the path difference, $a - b$, we have path-specific Green's functions for each node. (c) The top panel shows the theoretical waveforms for two point sources (red for the northern node and green for the southern node) separated by 40 km and recorded at six regional distances. The bottom panel shows a comparison of the theoretical Green's functions of the northern node (green waveforms) and the path difference corrected signals (red waveforms) using the southern node as an EGF corrected to the northern node position. Stations are selected from those used in LFM inversion, with station names, azimuths, and distances marked ahead of each trace.

[32] 2. A phase correction is applied to each frequency by the differential epicenter distances and the theoretical Love and Rayleigh wave fundamental mode dispersion curves.

[33] 3. An inverse Fourier transform recovers the time domain signal from the corrected spectra.

[34] 4. A geometrical spreading factor, involving the square root of the differential epicentral distance, and an azimuthal radiation ratio are applied to the corrected Green's functions to adjust the amplitudes.

[35] As a test, two theoretical Green's functions were calculated for two nodes separated by 40 km. Then the waveforms for one node are corrected to the other node location using the differential path distances to several stations using the theoretical dispersion curve. The corrected Green's functions show good phase consistency with the Green's functions at the target node (Figure 8c). Any small amplitude discrepancies due to radiation pattern differences will not impact our conclusions about rupture velocity since the rupture velocity is mainly related to the timing or phase, in contrast with the absolute moment scale, which is more related to the waveform amplitude.

[36] The EGF correction accounts for the propagation on the main portion of the raypath for ~1000 km. However, a model-based correction is still needed to adjust the differential travel times near the source. One concern about the phase correction accuracy comes from uncertainty of the dispersion curves. The corrected Green's functions span 160 km along the fault strike, involving 0–135 km differential travel distances from the EGF. If our reference model is inaccurate, the northernmost node will suffer the maximum phase error. Assuming a maximum 135 km differential travel distance, the differential travel time is ~45 s at 0.05 Hz and ~30 s at 0.01 Hz. If we assume our reference model has an average error of 5%, then the travel time discrepancy introduced by the reference model uncertainty is ~2 s for 0.05 Hz and ~1.5 s for 0.01 Hz. Thus, our phase correction suffers at most 10% phase error and will be much smaller for the dominant frequency and the majority of nodes.

5.2. Model Parameterization

[37] Because no depth correction is applied to the EGF (the vertical finiteness of that event is uncertain), the inversion with EGF-corrected Green's functions is constrained to a "linear" fault model (LFM), without along-dip parameterization. The LFM is parameterized with the same along-strike parameters as the FFM, with 16 nodes having increments of 10 km extending 160 km along strike. The source is again selected to be the fifth node along strike from the south, allowing for a northward dominated rupture. The same multi time-window inversion is applied to the LFM, in which the source time function of each node is parameterized the same as in the FFM inversion.

5.3. Regional Surface Wave Data Sets

[38] Fifty-six Love wave (G1) records and 46 Rayleigh wave (R1) records at regional distances <1000 km are used in a joint inversion. An azimuth window is applied to preselect the data, to exclude stations within 30° from Love or Rayleigh wave nodal directions. We do not invert the data jointly with near-regional data or teleseismic data, given the different nature of the Green's functions. G1 signals are extracted from transverse components and R1 signals from vertical components for both the EGF and main shock. A theoretical dispersion curve of the fundamental G1 and R1 modes is computed from the local 1-D model. A 1000 s long time window is used to extract the raw data and Green's functions, starting from the earthquake initiation time. A group velocity

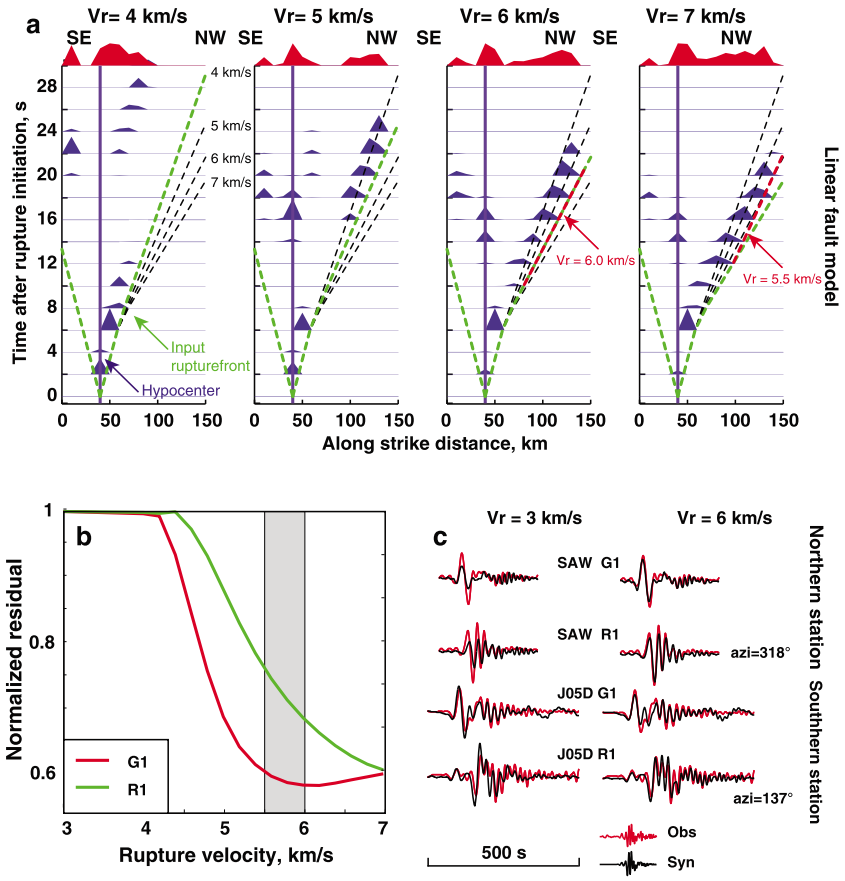

Figure 9. (a) Along-strike moment rate patterns for linear-fault model (LFM) inversions with different rupture velocities, *Vr*. The inversion used 46 Rayleigh wave (R1) and 56 Love wave (G1) recordings. The hypocenter is marked with a blue line. Prescribed rupture fronts are shown as green-dashed lines. Reference rupture front curves for *Vr* = 4, 5, 6, and 7 km/s are shown as black dashed lines. For the *Vr* = 6.0 km/s and 7.0 km/s cases, the inverted solutions yield effective rupture velocity of 5.5 km/s and 6.0 km/s, respectively, marked with red dashed lines. (b) Trade-off curves for normalized inversion residual versus input rupture velocity. Red and green curves are residuals of G1 and R1 waves, respectively, normalized by the maximum residual at *Vr* = 3 km/s. The range of preferred rupture velocity (5.5–6.0 km/s) is shaded. (c) Examples of waveform fitting improvements when model rupture velocity increases from 3 km/s to 6 km/s. The observed and predicted waveforms are plotted in red and black, respectively. The complete set of waveform fits for the LFM are shown in Figures S2a and S2b.

window from 3 to 5 km/s is used to isolate the energy of the fundamental mode wave packages. Both Green's functions and data are filtered with a causal band-pass filter, with corner frequencies at 0.01 and 0.05 Hz.

[39] For each node, the corrected Green's functions are used in a nonnegative least squares inversion, which imposes the assumption that the focal mechanism produced in the main shock inversion is identical to that of the EGF, so no rake variation along strike is allowed. Similar to FFM inversion, when imposing a *Vr*, the inversion is constrained to the solution space with rupture velocity no larger than that *Vr*.

5.4. Inversion Results

[40] For *Vr* of 4 to 5 km/s, the source time function of each node is delimited by the specified rupture front and the length of the slip distribution increases with *Vr*, indicating underestimation of *Vr*. In contrast, for *Vr* of 6 to 7 km/s, the source functions indicate lower apparent rupture velocities in the range 5.5 to 6.0 km/s and the inversion residual waveform mismatch does not reduce much with increasing *Vr* (Figure 9). All waveform fits are shown in Figures S2a and S2b. The moment distribution on the linear fault model is very similar for inversions with *Vr* = 6.0 km/s and 7.0 km/s, with strong similarity to the slip pattern of FFM inversions that used completely independent data sets for *Vr* = 6.0 km/s and 7.0 km/s. The preferred LFM has *Vr* = 6.0 km/s, as for the FFM inversion, with rupture extending ~30 km to the south and ~100 km to the north of the hypocenter. Regions of large slip are located ~10 km and ~70 km north of the hypocenter, similar to what was found in the FFM inversions. The total seismic moment for the LFM is 2.6×10^{20} Nm, giving a magnitude of $M_w = 7.54$.

[41] The peak-to-peak surface wave maximum amplitude ratio between the main event and the EGF event shows significant contrast between the northern and southern stations (Figure 10) due to the rupture propagation effect. At the northern stations, both Love and Rayleigh waves indicate an amplitude ratio of 800–1000, which is close to the moment ratio between the main event and the EGF event. At the southern

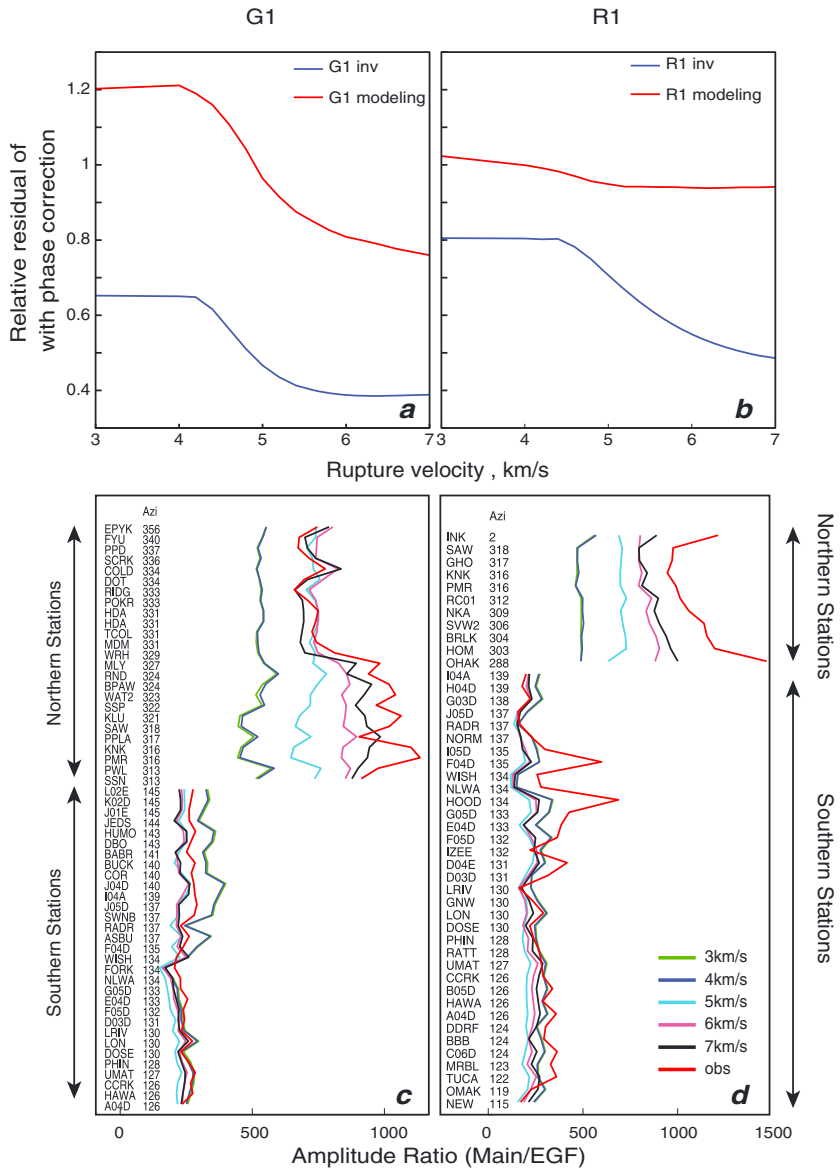

Figure 10. The misfit residual versus *Vr* trade-off curves produced by full waveform linear fault model (LFM) inversions (blue curves) and finite-fault model (FFM) based forward predictions (red curves), using EGF signals at each station corrected for grid location using theoretical phase velocities for (a) Love waves and (b) Rayleigh waves. Residuals are normalized by the squared norm of the waveforms. (c) Love wave and (d) Rayleigh wave peak-to-peak amplitude ratios (main event/EGF event) at each station are plotted for synthetic and observed (red) G1 and R1 waves. Stations are sorted by their azimuths. Amplitude ratios for input rupture velocities of 3 to 7 km/s are compared with observations. Station names and azimuths are indicated to the left of the curves.

stations, the amplitude ratio is ~300, which is 3 to 4 times smaller than for the northern stations as a consequence of the northward directivity. The amplitude ratio was also calculated between the LFM inversion synthetics and the EGF surface waves. The amplitudes are generally well matched at southern stations for different *Vr*, but the fit improved with increasing rupture velocity for the northern stations. The Love wave amplitude ratio could be fit well with a rupture velocity of 6 or 7 km/s; however, these models underestimate the Rayleigh wave amplitudes by about ~20%. Part of the differential fitting behavior may be attributed to the different station distributions between Love and Rayleigh waves used in the inversion. The Love wave stations are distributed along both sides of the strike direction and are particularly sensitive to the in-plane rupture propagation; however, nodal along-strike stations are removed for the Rayleigh waves, so the Rayleigh waves are less sensitive to the rupture propagation. Only a few northern stations are used in the LFM inversions for Rayleigh waves; thus, the inversion results are mainly controlled by the Love waves. The preferred rupture velocity is primarily determined from the Love wave trade-off curve. The strong amplitude variations are generally compatible with generic modeling of supershear rupture [e.g., *Bizzarri and Spudich*, 2008; *Bizzarri et al.*, 2010] and clearly demonstrate the enhanced

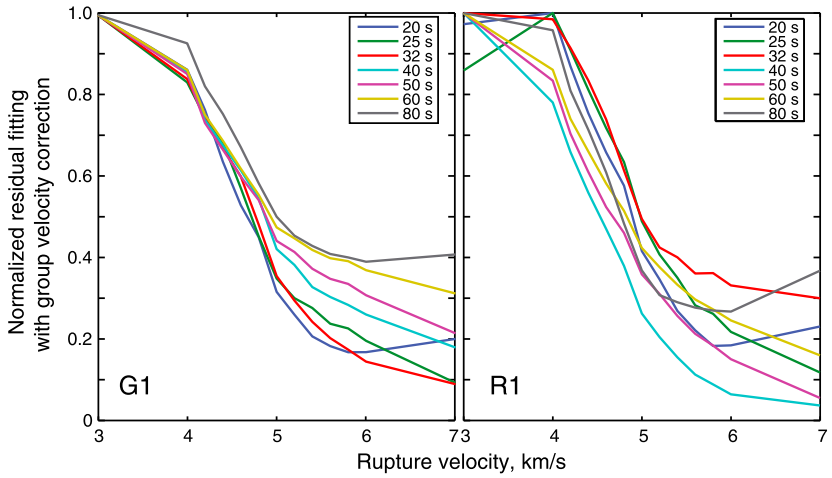

Figure 11. Trade-off curves of forward modeling normalized misfits to narrow-band Love wave (G1) and Rayleigh wave (R1) signals for varying rupture velocities for different central period passbands, plotted with different colors. Observed average group velocity curves provide group velocity corrections for the corresponding narrow-band filtered EGF signals for differential path lengths from each grid node to each station. The finite-fault model (FFM) inversion results for each *Vr* are used to predict the narrow-band filtered main shock waveforms with the corrected EGF signals being used as Green's functions along the fault.

seismic shaking hazard presented by supershear faulting of strike-slip events.

6. Finite-Fault Model and Linear Fault Model Comparison

[42] A forward modeling technique was applied using FFM results to predict waveforms using the phase-velocity-corrected empirical Green's functions. We computed a corrected EGF (c-EGFs) database for each grid of the FFM, then the moment distribution of FFM results for a given rupture velocity is used to weight the c-EGFs and sum them to give a simulated waveform. This yields broadband waveforms for comparison with each observation that allow direct comparison between the FFM and LFM results. The waveform misfit residuals are normalized by the square norm of the observed waveforms, indicating the percentage of misfit signal (Figures 10a and 10b). The forward modeling approach gives higher residuals than the inversion because the inversion more fully explores the source parameter space, improving the waveform fitting. The Love wave modeling approach produces similar decreasing residuals as rupture velocity in the FFM increases to 5.5–6.0 km/s. The Rayleigh wave modeling residuals are less pronounced but also decrease as *Vr* increases. In both modeling and inversion results, the residual decrease as *Vr* increases is clear, indicating consistent supershear rupture velocities.

[43] The rupture velocity estimated from the residual trade-off curves of both the FFM and LFM inversions is in the range 5.5–6.0 km/s. The *Vr* could also be directly measured from the along-strike moment distributions. The along-strike moment distribution shows a similar pattern between the LFM and depth-stacked FFM results. When the input *Vr* is smaller than the real *Vr*, the moment abuts the allowed rupture front; when the input *Vr* is larger than the true *Vr*, the inversion tends to define an effective rupture velocity that is lower than the maximum allowed. For $Vr = 6$ km/s and 7 km/s, the effective rupture velocity is measured as 5.5 to 6.0 km/s from the LFM inversion results (Figure 9a) and the same values are found for FFM inversions. This is consistent with the rupture velocity estimated from the waveform mismatch trade-off curves (Figures 7c and 9b). It is important to note that minor moment still abuts the allowed rupture front for $Vr = 7.0$ km/s, so tracing the first nonzero moment will recover the input rupture velocity of $Vr = 7.0$ km/s. How to select the initial significant moment on each node presents challenges for evaluating the moment rate functions of each node objectively. Measuring the rupture velocity gives an indication of how apparent rupture velocity differs from the input rupture velocity but may not provide a precise measurement of true rupture velocity.

[44] Local rupture velocity varies over the northern segment, but detailed measurement for each segment does not yield consistent rupture velocity patterns for different inversions. Such rupture velocity details may not be resolved stably in either FFM or LFM inversions, but the overall supershear rupture with an average rupture velocity of 5.5 to 6.0 km/s is robust.

7. Modeling With Group Velocity Corrections

[45] Waveform inversion of regional surface waves with the phase velocity correction may slightly suffer from reference velocity model inaccuracy since a theoretical dispersion curve is used for EGF correction. One technique that can eliminate reference model inaccuracy involves using empirical group velocity corrections, which relies on the measured group velocity at each station to compute a group arrival time shift for different passbands. Our group velocity correction procedure follows these steps:

[46] 1. Measure the group velocity for each path using the peak amplitude arrival time of different narrow band-pass filters, obtaining group velocity dispersion curves for regional

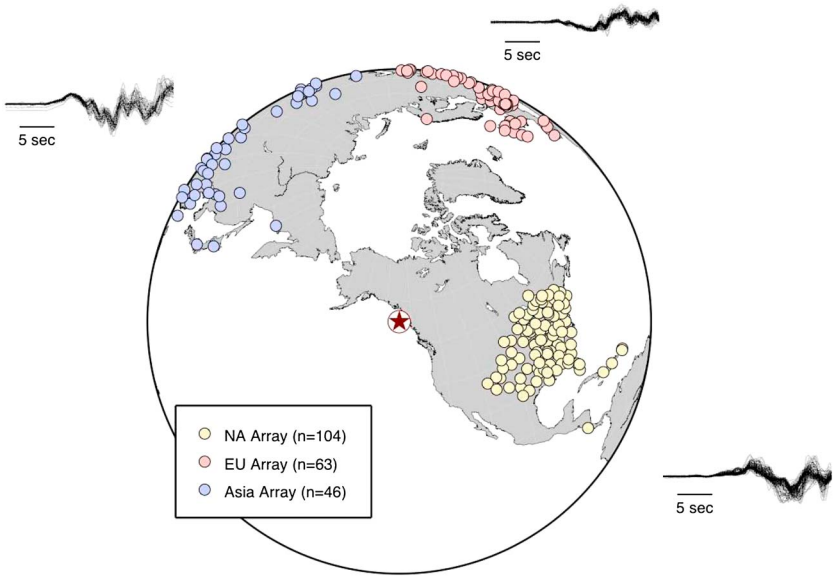

Figure 12. Locations of seismic stations recording teleseismic *P* waves used to back-project the space-time history of short-period radiation for the 2013 Craig earthquake. The stations are grouped into three arrays based on azimuth from the source and the data from each array are back-projected separately. Unfiltered, vertical component *P* waves from each array are shown along the plot border after being aligned and normalized with a multichannel cross-correlation algorithm. The high signal coherence of the broadband *P* arrivals allows stable initial alignment of the short-period arrivals.

Love and Rayleigh waves. Dispersion curves are extracted from both main shock and EGF signals, and we find good consistency.

[47] 2. Band-pass the EGF waveform with a sequence of narrow frequency windows that produce EGF wave packets at different band passes.

[48] 3. Apply station and wave-type-specific time correction to the multiband-passed EGF wave packets, correcting for the differential propagation lengths from each node on the main shock model relative to the EGF path lengths.

[49] 4. Use surface wave geometric spreading factors to correct for differences in propagation length of the Green's function databases.

[50] In this way, the EGF signals are corrected to any location in the near source region, giving a corrected EGF (c-EGF) database for a range of narrow band filtered windows. The seismic moment of the FFM results for different assumed *Vr* is then used to produce synthetics for a given passband using the c-EGF signals along the fault model. Comparison of the modeled and observed waveforms for different band passes provides an evaluation of the FFM result reliability for an independent data set. The waveform-mismatch residual versus FFM *Vr* trade-off curves for rupture velocities from 3 to 7 km/s are computed (Figure 11). A consistent residual reduction with increasing rupture velocity from $Vr = 3$ to 7 km/s is found over all passbands from 20 s to 100 s. The minimum residual is found for $Vr = 5$ to 6 km/s, which produces an 80%–60% residual reduction relative to the residual for $Vr = 3$ km/s.

[51] This procedure relies only on observed information, such as the EGF waveforms and the measured group velocity dispersion curves, so it reduces uncertainty introduced by a reference model other than that affecting the FFM. The residual trade-off curve provides an independent and objective evaluation of the FFM results for a distinct data set, giving supportive evidence for a supershear rupture velocity.

8. Back Projection of Teleseismic *P* Waves

[52] Teleseismic *P* waves from three regional groupings of global broadband seismometers were back projected to the source region [*Xu et al.*, 2009] in order to image the short-period rupture properties of the 5 January 2013 Craig, Alaska earthquake. In each case, the NEIC location of 55.394°N, 134.650°W, h = 7.1 km, 08:58:19 UTC was used as a reference for aligning the waveforms. The source area was gridded in increments of 0.1° in latitude and longitude and depth was held constant at the nominal hypocentral value. Power was calculated from a 10 s long, tapered window that slides along beams created with fourth-root stacking. Traces were band-pass filtered between 0.5 and 2 s prior to being stacked, and the AK135 reference Earth model was used to calculate travel times.

[53] All the data used in the back-projection analysis were downloaded from the IRIS DMC. A multichannel cross-correlation analysis [*VanDecar and Crosson*, 1990] was used to select similar waveforms. For the Asia array 46 traces with mean correlation coefficients above 0.85 were retained, for the North America array 104 traces with mean correlation coefficients above 0.87 were retained, and for the Europe array 63 traces with mean correlation coefficients above 0.8 were retained (Figure 12). The cross correlations were performed on unfiltered, vertical component velocity waveforms using a window that started 5 s before the theoretical *P* arrival and extended for either 15 or 20 s.

[54] Time-integrated images of the back-projected power for each station array are shown in Figure 13. Animations of the time-varying sequences are in Animation S1. Comparison of the Asian back projections for the main shock and EGF event

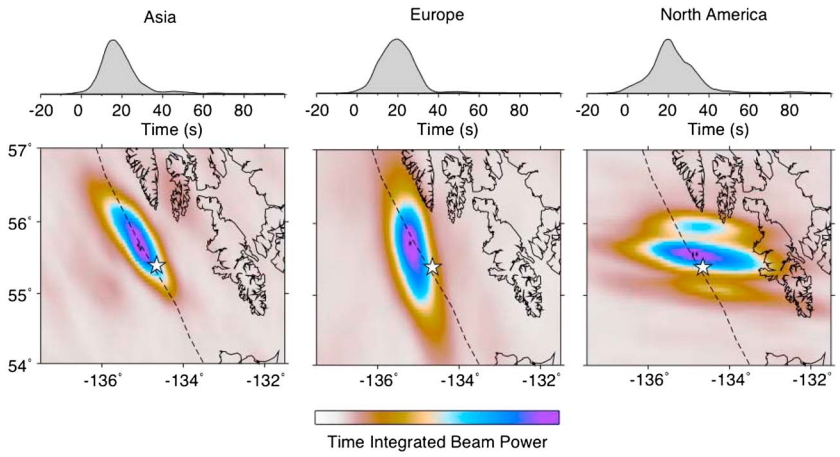

Figure 13. Time-integrated images from back-projection results for the three teleseismic arrays considered in this study. In each panel, the star represents the epicenter and the dashed line represents the boundary between the North American and Pacific plates. All three analyses indicate a dominantly northern rupture, with energy extending at least as far north as 56° N, similar to the extent of aftershocks occurring in the first month after the main shock (Figure 1). Weaker energy is observed just to the south of the epicenter. The time evolution of peak beam power shown atop the panels is influenced by a 10 s long smoothing window and the actual duration of short-period energy release is less than 40 s.

is shown in Animation S2 to convey the degree of space-time smearing of the image for a relative point-source event (the EGF), compared to the finite rupture of the main shock. The teleseismic back-projection images have limited resolution of rupture velocity, but are compatible with up to 6 km/s.

9. Discussion

[55] The seismic and geodetic ground motion analyses discussed here all indicate that the 2013 Craig earthquake had supershear rupture velocity in the range 5.5 to 6.0 km/s along the northern portion of the rupture and subshear rupture expansion to the south. Theoretical and experimental studies of bimaterial mode II ruptures, with a velocity contrast across the fault, indicate that supershear rupture will be more likely in the direction of motion of the high seismic velocity side of the fault, with a velocity slightly lower than the *P* wave velocity of the slow side [*Xia et al*., 2005; *Cochard and Rice*, 2000]. For the Queen Charlotte Fault (Figure 1), the fast side is the oceanic plate, which is moving northward, consistent with observed northward supershear rupture direction. Our estimates of rupture velocity 5.5 to 6.0 km/s approach the *P* wave velocity of 6.6 km/s in the midcrust (10 km) of the continental side [*Horn et al*., 1984].

[56] In a few previous studies of supershear rupture, aftershocks are inferred to be activated on off-fault branches, and there is relatively low aftershock production on the main fault plane as a result of large stress drop [*Bouchon and Karabulut*, 2008]. The Mach waves can also cause off-fault damage patterns that could be diagnostic of supershear rupture [*Bhat et al*., 2007], but this will not be accessible for an offshore event. For the 2013 Craig earthquake, most aftershocks locate along the plate boundary, but some are located away from the trace of the Queen Charlotte Fault. Three aftershocks with $M_w > 4.5$ have focal mechanism determinations (Figure 1), two of which are consistent with rupture on the Queen Charlotte Fault, whereas the largest aftershock, M_w 5.9 event on 31 January 2013 (Figure 1), ruptured a differently oriented fault. It is important to notice that the previous supershear events mostly involve intraplate or continental events, where complex stress and structure heterogeneities may be present near the fault zone. For the Craig interplate event, the shear loading is released along a major plate boundary. The aftershock behavior may be affected by the strong material contrast across the ocean/continent boundary or the absence of preexisting fault branches.

[57] It is also indicated in previous studies that supershear rupture may be related to a full stress release that prevents aftershocks on the main fault plane [*Bouchon and Karabulut*, 2008]. Theoretically, the supershear rupture may be related to a high stress drop relative to the strength drop near the crack tip [*Andrews*, 1976]. For our finite fault model of the 2013 Craig event, it is hard to resolve dynamic stress drops, but the average static stress drop is approximately 9 MPa, measured from the final rupture pattern. Such a stress drop is about 3 times the average stress drop of interplate events and close to typical intraplate event stress drop [*Kanamori and Anderson*, 1975]. It is hard to tell whether this slightly elevated stress drop is complete because the prestress state is not known. Aftershocks do occur along the primary slip area laterally, but these could locate beneath or above the coseismic slip area given the uncertainties in depth distribution. Further relocation efforts will be needed to determine whether any aftershocks colocate with the coseismic slip regions. This would help to determine whether total stress drop occurred in this supershear event.

[58] The 2013 Craig, Alaska event is the first oceanic interplate event reported to have involved supershear rupture, and it is the first offshore event for which multiple data sets independently indicate supershear rupture. Occurrence of supershear rupture has been associated with straight fault segments and termination of supershear with fault bending and splaying [*Das*, 2007; *Robinson et al*., 2010; *Bouchon et al*., 2010]. The Queen Charlotte Fault does appears to be relatively straight in the northern supershear rupture area, but the geometry is not known precisely and there is not a

readily apparent explanation for the termination of rupture in the north other than it is near the southern end of the rupture zone for the 30 July 1972 Sitka, Alaska (M_w 7.6) earthquake, so the prestress may be low north of the rupture zone. Stress heterogeneity on the fault likely plays a role in enabling and delimiting supershear [*Schmedes et al*., 2010], but the offshore location of the fault limits our understanding of fine structure that might be manifestations of such stress heterogeneity. While measurements very close to the fault were not possible, the combined geodetic and seismic observations for the 2013 event still give one of the most robust characterizations of supershear rupture to date.

10. Conclusions

[59] The 2013 M_w 7.5 Craig, Alaska event is found to have had a supershear rupture velocity using several independent modeling and inversion techniques.

[60] *Sg* and *Sn* pre-hypocentral arrivals have been detected with a EGF reference time technique and indicate that the northward rupture velocity of >4.5 km/s for the Craig event surpassed the crustal and upper mantle shear velocity. The northward supershear rupture process produced significant short-period shaking enhancement, almost 1 order of magnitude larger to the north, consistent with models of *Bizzarri and Spudich* [2008].

[61] Finite-fault model inversions with regional geodetic/seismic and teleseismic observations and linear fault model inversions using regional seismic observations indicate a rupture velocity of 5.5 to 6.0 km/s. Forward modeling procedures, using theoretical phase velocity or group velocity corrections, indicate significant waveform fitting residual decreases with increasing rupture velocity. The rupture velocity is consistent with that resolved by the inversions.

[62] The 2013 Craig, Alaska event rupture extends about 100 km northward from the hypocenter, with about 80 km of supershear rupture. Two significant energy release peaks have been identified along the strike direction located 20 km and 70 km north of the hypocenter. The rupture initially extended ~20–30 km to the north and south with subshear rupture. The northward supershear rupture direction may be related to the strong material contrast across the continental-oceanic plate boundary.

[63] **Acknowledgments.** We thank Emily Brodsky and Hiroo Kanamori for exchanging ideas on supershear rupture. Eric Dunham and an anonymous reviewer provided helpful comments. We thank Charles Ammon for providing his group velocity analysis code. The Incorporated Research Institutions for Seismology data management center and the Canadian National Seismic Network data center provided seismic data seismic data from global stations and the Alaska Regional Seismic Network. GPS data were provided by the EarthScope Plate Boundary Observatory data center. This work was supported in part by NSF under grants EAR-1245717 (T.L.) and EAR-0911764 (J.F.).

References

Andrews, D. J. (1976), Rupture velocity of plane strain shear cracks, *J. Geophys. Res.*, *81*(32), 5679–5687.

Andrews, D. J. (1985), Dynamic plane-strain shear rupture with a slip-weakening friction law calculated by a boundary integral method, *Bull. Seismol. Soc. Am.*, *75*(1), 1–21.

Andrews, D. J. (2010), Ground motion hazard from supershear rupture, *Tectonophysics*, *493*(3–4), 216–221.

Antolik, M., R. E. Abercrombie, and G. Ekström (2004), The 14 November 2001 Kokoxili (Kunlunshan), Tibet, Earthquake: Rupture transfer through a large extensional step-over, *Bull. Seismol. Soc. Am.*, *94*, 1173–1194.

Aochi, H., V. Durand, and J. Douglas (2011), Influence of supershear earthquake rupture models on simulated near-source ground motion from the 1999 Izmit, Turkey, earthquake, *Bull. Seismol. Soc. Am.*, *101*(2), 726–741.

Archuleta, R. J. (1984), A faulting model for the 1979 Imperial Valley earthquake, *J. Geophys. Res.*, *89*(B6), 4559–4585.

Bhat, H. S., R. Dmowska, G. C. P. King, Y. Klinger, and J. R. Rice (2007), Off-fault damage patterns due to supershear rupture with application to the 2001 M_w 8.1 Kokoxili (Kunlun) Tibet earthquake, *J. Geophys. Res.*, *112*, B06301, doi:10.1029/2006JB004425.

Birgören, G., H. Sekiguchi, and K. Irikura (2004), Rupture model of the 1999 Düzce, Turkey, earthquake deduced from high and low frequency strong motion data, *Geophys. Res. Lett.*, *31*, L05610, doi:10.1029/2003GL019194.

Bizzarri, A., and P. Spudich (2008), Effects of supershear rupture speed on the high-frequency content of *S* waves investigated using spontaneous dynamic rupture models and isochrones theory, *J. Geophys. Res.*, *113*, B05304, doi:10.1029/2007JB005146.

Bizzarri, A., E. M. Dunham, and P. Spudich (2010), Coherence of Mach fronts during heterogeneous supershear earthquake rupture propagation: Simulations and comparison with observations, *J. Geophys. Res.*, *115*, B08301, doi:10.1029/2009JB006819.

Bouchon, M., and M. Vallée (2003), Observation of long supershear rupture during the magnitude 8.1 Kunlunshan earthquake, *Science*, *301*(5634), 824–826.

Bouchon, M., and H. Karabulut (2008), The aftershock signature of supershear earthquakes, *Science*, *320*(5881), 1323–1325.

Bouchon, M., M.-P. Bouin, H. Karabulut, M. N. Toksöz, M. Dietrich, and A. J. Rosakis (2001), How fast is rupture during an earthquake? New insights from the 1999 Turkey earthquakes, *Geophys. Res. Lett.*, *28*(14), 2723–2726.

Bouchon, M., M. N. Toksöz, H. Karabulut, M.-P. Bouin, M. Dietrich, M. Aktar, and M. Edie (2002), Space and time evolution of rupture and faulting during the 1999 İzmit (Turkey) earthquake, *Bull. Seismol. Soc. Am.*, *92*(1), 256–266.

Bouchon, M., H. Karabulut, M.-P. Bouin, J. Schmittbuhl, M. Vallée, R. Archuleta, S. Das, F. Renard, and D. Marsan (2010), Faulting characteristics of supershear earthquakes, *Tectonophysics*, *493*(3–4), 244–253.

Bouin, M. P., M. Bouchon, H. Karabulut, and M. Aktar (2004), Rupture process of the 1999 November 12 Düzce (Turkey) earthquake deduced from strong motion and Global Positioning System measurements, *Geophys. J. Int.*, *159*(1), 207–211.

Burridge, R. (1973), Admissible speeds for plane-strain self-similar shear cracks with friction but lacking cohesion, *Geophys. J. R. Astron. Soc.*, *35*(4), 439–455.

Burridge, R., G. Conn, and L. B. Freund (1979), The stability of a rapid mode II shear crack with finite cohesive traction, *J. Geophys. Res.*, *85*(B5), 2210–2222.

Choy, G. L., and J. Boatwright (2004), Radiated energy and the rupture process of the Denali Fault earthquake sequence of 2002 from broadband teleseismic body waves, *Bull. Seismol. Soc. Am.*, *94*(6B), S269–2S77.

Cochard, A., and J. R. Rice (2000), Fault rupture between dissimilar materials: Ill-posedness, regularization, and slip-pulse response, *J. Geophys. Res.*, *105*(B11), 25,891–25,907.

Das, S. (2007), The need to study speed, *Science*, *317*(5840), 905–906.

Day, S. M. (1982), Three-dimensional simulation of spontaneous rupture: The effect of nonuniform prestress, *Bull. Seismol. Soc. Am.*, *72*(6), 1881–1902.

Dunham, E. M. (2005), The dynamics and near-source ground motion of supershear earthquakes, PhD thesis, University of California, Santa Barbara, 225 pp.

Dunham, E. M., and R. J. Archuleta (2004), Evidence for a supershear transient during the 2002 Denali Fault earthquake, *Bull. Seismol. Soc. Am.*, *94*(6B), S256–S268, doi:10.1785/0120040616.

Dunham, E. M., and H. S. Bhat (2008), Attenuation of radiated ground motion and stresses from three-dimensional supershear ruptures, *J. Geophys. Res.*, *113*, B08319, doi:10.1029/2007JB005182.

Dunham, E. M., P. Favreau, and J. M. Carlson (2003), A supershear transition mechanism for cracks, *Science*, *299*(5612), 1557–1559.

Ellsworth, W. L., M. Celebi, J. R. Evans, E. G. Jensen, R. Kayen, M. C. Metz, D. J. Nyman, J. W. Roddick, P. Spudich, and C. D. Stephens (2004), Near-field ground motion of the 2002 Denali Fault, Alaska, earthquake recorded at pump station 10, *Earthquake Spectra*, *20*(3), 597–615.

Festa, G., and J.-P. Vilotte (2006), Influence of the rupture initiation on the intersonic transition: Crack-like versus pulse-like modes, *Geophys. Res. Lett.*, *33*, L15320, doi:10.1029/2006GL026378.

Frankel, A. (2004), Rupture process of the M 7.9 Denali Fault, Alaska, earthquake: Subevents, directivity, and scaling of high-frequency ground motions, *Bull. Seismol. Soc. Am.*, *94*(6B), S234–S255, doi:10.1785/0120040612.

Freund, L. B. (1979), The mechanics of dynamic shear crack propagation, *J. Geophys. Res.*, *84*(B5), 2199–2209.

Fu, Y., and J. T. Freymueller (2012), Seasonal and long-term vertical deformation in the Nepal Himalaya constrained by GPS and GRACE measurements, *J. Geophys. Res.*, *117*, B03407, doi:10.1029/2011JB008925.

Hartzell, S. H., and T. H. Heaton (1983), Inversion of strong ground motion and teleseismic waveform data for the fault rupture history of the 1979 Imperial Valley, California, earthquake, *Bull. Seismol. Soc. Am.*, *73*(6A), 1553–1583.

Horn, J. R., R. M. Clowes, R. M. Ellis, and D. N. Bird (1984), The seismic structure across an active oceanic/continental transform fault zone, *J. Geophys. Res.*, *89*(B5), 3107–3120.

Kanamori, H., and D. L. Anderson (1975), Theoretical basis of some empirical relations in seismology, *Bull. Seismol. Soc. Am.*, *65*(5), 1073–1095.

Kaneko, Y., and N. Lapusta (2010), Supershear transition due to a free surface in 3-D simulations of spontaneous dynamic rupture on vertical strike-slip faults, *Tectonophysics*, *493*(3–4), 272–284.

Kikuchi, M., H. Kanamori, and K. Satake (1993), Source complexity of the 1988 Armenian earthquake: Evidence for a slow after-slip event, *J. Geophys. Res.*, *98*(B9), 15,797–15,808.

Konca, A. O., S. Leprince, J.-P. Avouac, and D. V. Helmberger (2010), Rupture process of the 1999 M_w 7.1 Duzce earthquake from joint analysis of SPOT, GPS, InSAR, strong-motion, and teleseismic data: A supershear rupture with variable rupture velocity, *Bull. Seismol. Soc. Am.*, *100*(1), 267–288.

Lawson, C. L., and R. J. Hanson (1995), *Solving Least Squares Problems, Classics in Applied Mathematics*, vol. 15, pp. 337, Society for Industrial Mathematics, Englewood Cliffs, N. J.

Lay, T., L. Ye, K. Kanamori, Y. Yamazaki, K. F. Cheung, K. Kwong, and K. D. Koper (2013), The October 28, 201 M_w 7.8 Haida Gwaii underthrusting earthquake and tsunami: Slip partitioning along the Queen Charlotte fault transpressional boundary, *Earth Planet. Sci. Lett.*, *375*, 57–70, doi:10.1016/j.epsl.2013.05.005.

Liu, Y., and N. Lapusta (2008), Transition of mode II cracks from sub-Rayleigh to intersonic speeds in the presence of favorable heterogeneity, *J. Mech. Phys. Solids*, *56*(1), 25–50.

Mello, M., H. S. Bhat, A. J. Rosakis, and H. Kanamori (2010), Identifying the unique ground motion signatures of supershear earthquakes: Theory and experiments, *Tectonophysics*, *493*(3–4), 297–326.

Mena, B., L. A. Dalguer, and P. M. Mai (2012), Pseudodynamic source characterization for strike-slip faulting including stress heterogeneity and supershear ruptures, *Bull. Seismol. Soc. Am.*, *102*(4), 1654–1680, doi:10.1785/0120110111.

Meng, L., J.-P. Ampuero, J. Stock, Z. Duputel, Y. Luo, and V. C. Tsai (2012), Earthquake in a maze: Compressional rupture branching during the 2012 M_w 8.6 Sumatra earthquake, *Science*, *337*(6095), 724–726, doi:10.1126/science.1224030.

Morozov, I. B., S. B. Smithson, L. S. Hollister, and J. B. Diebold (1998), Wide-angle seismic imaging across accreted terranes, southeastern Alaska and western British Columbia, *Tectonophysics*, *299*(4), 281–296.

Olsen, K. B., R. Madariaga, and R. J. Archuleta (1997), Three-dimensional dynamic simulation of the 1992 Landers earthquake, *Science*, *278*, 834–838.

Passelègue, F. X., A. Schubnel, S. Nielsen, H. S. Bhat, and R. Madariaga (2013), From sub-Rayleigh to supershear ruptures during stick–slip experiments on crustal rocks, *Science*, *340*(6137), 1208–1211.

Robinson, D. P., C. Brough, and S. Das (2006), The M_w 7.8, 2001 Kunlunshan earthquake: Extreme rupture speed variability and effect of fault geometry, *J. Geophys. Res.*, *111*, B08303, doi:10.1029/2005JB004137.

Robinson, D. P., S. Das, and M. P. Searle (2010), Earthquake fault superhighways, *Tectonophysics*, *493*, 236–243.

Rosakis, A. J., O. Samudrala, and D. Coker (1999), Cracks faster than the shear wave speed, *Science*, *284*(5418), 1337–1340.

Schmedes, J., R. J. Archuleta, and D. Lavallée (2010), Dependency of supershear transition and ground motion on the autocorrelation of initial stress, *Tectonophysics*, *493*(3–4), 222–235.

Sekiguchi, H., and T. Iwata (2002), Rupture process of the 1999 Kocaeli, Turkey, earthquake estimated from strong-motion waveforms, *Bull. Seismol. Soc. Am.*, *92*(1), 300–311.

Spudich, P., and E. Cranswick (1984), Direct observation of rupture propagation during the 1979 Imperial Valley earthquake using a short baseline accelerometer array, *Bull. Seismol. Soc. Am.*, *74*(6), 2083–2114.

Vallée, M., and E. M. Dunham (2012), Observation of far-field Mach waves generated by the 2001 Kokoxili supershear earthquake, *Geophys. Res. Lett.*, *39*, L05311, doi:10.1029/2011GL050725.

VanDecar, J. C., and R. S. Crosson (1990), Determination of teleseismic relative phase arrival times using multi-channel cross-correlation and least squares, *Bull. Seismol. Soc. Am.*, *80*(1), 150–169.

Walker, K. T., and P. M. Shearer (2009), Illuminating the near-sonic rupture velocities of the intracontinental Kokoxili M_w 7.8 and Denali fault M_w 7.9 strike-slip earthquakes with global *P* wave back projection imaging, *J. Geophys. Res.*, *114*, B02304, doi:10.1029/2008JB005738.

Wang, D., and J. Mori (2012), The 2010 Qinghai, China, earthquake: A moderate earthquake with supershear rupture, *Bull. Seismol. Soc. Am.*, *102*(1), 301–308.

Wang, D., J. Mori, and T. Uchide (2012), Supershear rupture on multiple faults for the M_w 8.6 Off Northern Sumatra, Indonesia earthquake of April 11, 2012, *Geophys. Res. Lett.*, *39*, L21307, doi:10.1029/2012GL053622.

Xia, K., A. J. Rosakis, and H. Kanamori (2004), Laboratory earthquakes: The sub-Rayleigh-to-supershear rupture transition, *Science*, *303*(5665), 1859–1861.

Xia, K., A. J. Rosakis, H. Kanamori, and J. R. Rice (2005), Laboratory earthquakes along inhomogeneous faults: Directionality and supershear, *Science*, *308*(5722), 681–684.

Xu, Y., K. D. Koper, O. Sufri, L. Zhu, and A. R. Hutko (2009), Rupture imaging of the M_w 7.9 12 May 2008 Wenchuan earthquake from back projection of teleseismic *P* waves, *Geochem., Geophys., Geosyst.*, *10*(4), Q04006, doi:10.1029/2008GC002335.

Yue, H., and T. Lay (2013), Source rupture models for the M_w 9.0 2011 Tohoku earthquake from joint inversions of high rate geodetic and seismic data, *Bull. Seismol. Soc. Am.*, *103*(2B), 1242–1255.

Yue, H., T. Lay, and K. Koper (2012), En échelon and orthogonal fault ruptures of the 11 April 2012 great intraplate earthquakes, *Nature*, *490*, 245–249, doi:10.1038/nature11492.

Yue, H., T. Lay, S. Schwartz, L. Rivera, M. Protti, T. H. Dixon, S. Owen, and A. V. Newman (2013), The 5 September 2012 Costa Rica M_w 7.6 earthquake rupture process from joint inversion of high-rate GPS, strong-motion, and teleseismic *P* wave data and its relationship to adjacent plate boundary interface properties, *J. Geophys. Res. Solid Earth*, *118*, 5453–5466, doi:10.1002/jgrb.50379.

Zumberge, J. F., M. B. Heflin, D. C. Jefferson, M. M. Watkins, and F. H. Webb (1997), Precise point positioning for the efficient and robust analysis of GPS data from large networks, *J. Geophys. Res.*, *102*(B3), 5005–5017.